Local probe evidence supporting altermagnetism in $Co_{1/4}NbSe_2$

J. N. Graham,[1,*,†] T. J. Hicken,[1,*,‡] Resham Babu Regmi,[2,3] M. Janoschek,[1,4] I. Mazin,[5,6] H. Luetkens,[1] N. J. Ghimire,[2,3] and Z. Guguchia[1,§]

[1]*PSI Center for Neutron and Muon Sciences CNM, 5232 Villigen PSI, Switzerland*
[2]*Department of Physics and Astronomy, University of Notre Dame, Notre Dame, Indiana 46556, USA*
[3]*Stravropoulos Center for Complex Quantum Matter, University of Notre Dame, Notre Dame, Indiana 46556, USA*
[4]*Physik-Institut, Universität Zurich, Winterthurerstrasse 190, CH-8057 Zurich, Switzerland*
[5]*Department of Physics and Astronomy, George Mason University, Fairfax, Virginia 22030, USA*
[6]*Quantum Science and Engineering Center, George Mason University, Fairfax, Virginia 22030, USA*

(Received 8 December 2025; accepted 26 May 2026; published 30 June 2026)

Muon spin rotation (μ^+SR) was used to investigate the magnetic properties of cobalt-intercalated 2*H*-$NbSe_2$ ($Co_{1/4}NbSe_2$). $Co_{1/4}NbSe_2$ is predicted to be an altermagnet, and while neutron diffraction has proposed its magnetic structure, the microscopic details of this remain unclear. Therefore, a local probe investigation of the magnetism in $Co_{1/4}NbSe_2$ is essential. Our results reveal a sharp second-order transition to a full-volume-fraction, homogeneous magnetic order below $T_N = 168$ K. The moments are aligned antiparallel along the *c* axis, consistent with neutron diffraction and altermagnetism. μ^+SR reveals that the state remains stable under a *c*-axis magnetic field up to 0.78 T, with magnetization measurements suggesting that this robust regime extends to at least 5 T. Within the time sensitivity of μ^+SR, no precursor slow magnetic fluctuations were detected above T_N, which is important for interpreting the band splitting in the paramagnetic state reported by photoemission studies.

DOI: 10.1103/6898-s17c

I. INTRODUCTION

Altermagnetism is a recently identified magnetic state that bridges the gap between conventional ferromagnetism and antiferromagnetism [1–10]. An altermagnet features unique spin-splitting behavior, where time-reversal and crystal symmetries lead to momentum-dependent spin polarization without net magnetization. A magnetic structure consisting of two antiparallel spin sublattices is also consistent with antiferromagnetism; however, the imposition of specific crystal symmetries leads to altermagnetism. Altermagnets are predicted to exhibit intriguing properties, including a spin-polarized band structure, robustness against external magnetic perturbations, and an ability to sustain spin-polarized transport without an external magnetic field. As such, altermagnets hold promise for spintronic applications, offering advantages like efficient spincurrent generation and manipulation.

Several materials have been proposed as candidates for altermagnetism, where the specific crystal symmetries enable momentum-dependent spin splitting without a net magnetization. Currently, there is a pressing need to experimentally confirm altermagnetism in real materials. Among the possible candidates are transition-metal compounds like CrSb [11,12] and MnTe [13,14], which exhibit altermagnetic band structures.

Another promising class of materials are the intercalated transition-metal dichalcogenides (TMDs). TMDs encompass a wide variety of MX_2 materials [15–19] where a transition-metal layer (*M*) is sandwiched between two chalcogen layers (X = S, Se, or Te) [17,20]. One of the most studied TMD compositions is $NbSe_2$, which in bulk form (2*H* trigonal prismatic stacking) exhibits a superconducting ground state, with critical temperature $T_C = 7.2$ K, and develops a charge density wave (CDW) below $T_{CDW} = 33.5$ K [21–26]. Both transitions are greatly affected when approaching monolayer thickness, with the CDW increasing to an extraordinary 145 K as T_C is suppressed to 3 K [27]. 2*H*-$NbSe_2$ and related materials are highly tunable under strain [28], pressure [29,30], or external fields, making them attractive for spintronics and to study exotic quantum states.

Intercalation offers further control over the electronic and magnetic properties, allowing fine-tuning of band structures, spin textures, and exchange interactions [31,32]. In layered TMDs, magnetic intercalants can induce complex spin textures through spin-orbit coupling, electron correlation, and symmetry effects [33–40]. For example, two distinct magnetic phases can be produced by the cobalt intercalation of different concentrations [41]. Namely, when the concentration of the intercalant is $\frac{1}{3}$ ($Co_{1/3}NbSe_2$), the structure adopts the noncentrosymmetric $P6_322$ structure that induces

*These authors contributed equally to the work.
†Contact author: jennifer.graham@fysik.lu.se
‡Contact author: thomas.hicken@psi.ch
§Contact author: zurab.guguchia@psi.ch

Published by the American Physical Society under the terms of the Creative Commons Attribution 4.0 International license. Further distribution of this work must maintain attribution to the author(s) and the published article's title, journal citation, and DOI.

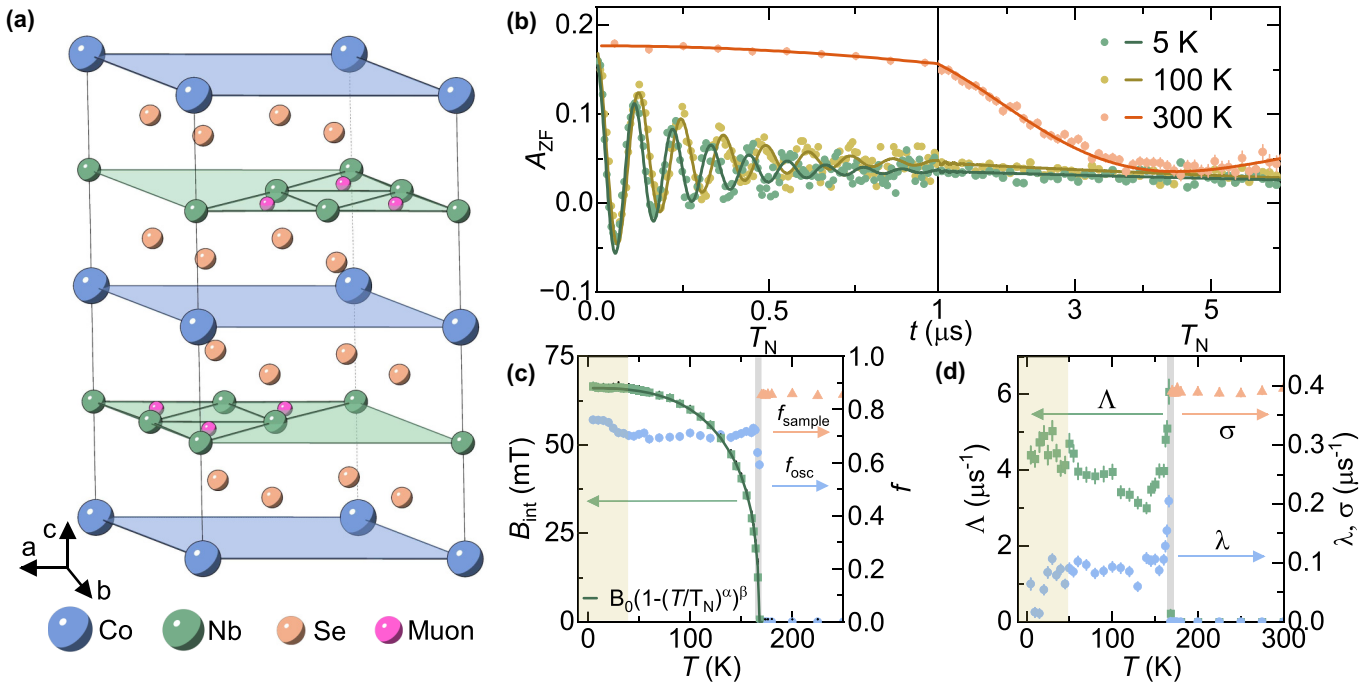


FIG. 1. Crystal structure, muon stopping site, and summary of μ^+SR experiments on $Co_{1/4}NbSe_2$. (a) $Co_{1/4}NbSe_2$ adopts the $P6_3/mmc$ crystal structure, which consists of cobalt atoms (blue) being intercalated between layers of $NbSe_2$ (green and peach, respectively). The muon stopping site (and equivalent positions, pink) lies within the $NbSe_2$ plane (green) at the center of the Nb triangle (lines are shown for clarity). (b) Raw spectra of zero-field μSR data at 5, 100, and 300 K. At low temperatures and short times, there is a fast relaxation and oscillations indicating long-range magnetic order. (c) Internal field $\mu_0 H_{int}$ (green), magnetic volume fraction f_{osc} (blue), and total fraction of the sample (peach) as a function of temperature. (d) Evolution of static, Λ (green), and dynamic, λ (blue), relaxation rates with temperature. Above T_N, data were modeled with a Gaussian Kubo-Toyabe function with relaxation, σ (peach). Yellow shaded region in panels (c) and (d) highlights the slight change in parameters below 30 K, where the magnetization exhibits a kink [6].

an incommensurate magnetic structure below $T_N = 28$ K [41]. Alternatively, when the intercalant concentration is $\frac{1}{4}$ ($Co_{1/4}NbSe_2$), the centrosymmetric $P6_3/mmc$ structure forms (as shown in Fig. 1), with moments aligning antiparallel along the c axis (two oppositely polarized ferromagnetic layers, akin to A-type antiferromagnetism) below $T_N = 168$ K [6].

$Co_{1/4}NbSe_2$ has recently garnered attention as a strong candidate for altermagnetism from density functional theory (DFT) calculations and experiments [1–6]. Experimental studies utilizing a combination of magnetometry and neutron scattering suggest that $Co_{1/4}NbSe_2$ adopts an A-type magnetic structure, with moments aligned antiparallel along the c axis [6]. This magnetic structure, with wave vector $\mathbf{q} = 0$, coupled with the lack of inversion center between two Co atoms from the intermediary $NbSe_2$ layers, is consistent with the symmetry requirements for an altermagnetic state in $Co_{1/4}NbSe_2$ below 168 K. Moreover, a recent study reports spin-Angle-Resolved Photoemission Spectroscopy (ARPES) [5] measurements showing that spin splitting mostly vanishes at T_N, but some residual spin splitting extends into the paramagnetic state, which is attributed to precursor magnetic fluctuations. Despite the reported magnetic properties, the microscopic details of the magnetic response, such as the magnetically ordered volume fraction, homogeneity of the magnetism, slow fluctuations both below and above T_N, and the stability of the magnetic structure have not yet been settled. Addressing these aspects is of paramount importance. In this paper, we tackle these questions using the highly sensitive local probe technique muon spin rotation (μ^+SR) combined with muon stopping site calculations and local field analysis.

II. RESULTS AND DISCUSSION

Zero-field (ZF) μ^+SR experiments were performed on the General-Purpose-Surface-Muon (GPS) instrument [42] at the Swiss Muon Source (SμS), Paul Scherrer Institute, on a c-axis aligned mosaic arrangement of single-crystal samples of $Co_{1/4}NbSe_2$ (see the Appendix). The initial muon spin was rotated 45° with respect to the muon momentum, providing sensitivity to both in- and out-of-plane magnetism. At high temperatures, the ZF μ^+SR spectra are well described by a Gaussian Kubo-Toyabe function [43] with a constant background, as expected for a system with no long-range magnetic order:

$$A_{ZF}^{GKT}(t) = \left(\frac{1}{3} + \frac{2}{3}(1-\sigma^2 t^2)\exp\left[-\frac{\sigma^2 t^2}{2}\right]\right) + A_{bkg}. \quad (1)$$

Here, σ/γ_μ represents the width of the local magnetic field distribution arising from nuclear moments. The background was estimated to be 17.0(3)%, which can be attributed to any muons not stopping in the sample (see the Appendix). To confirm the magnetic volume fraction, we also performed weak-transverse-field measurements, where a field is applied perpendicular to the initial muon spin direction. We find that

the muons attributed to stopping in the sample all stop in regions of long-range magnetic order, suggesting that, within experimental uncertainty, the full volume fraction is magnetically ordered below $T_N = 168$ K. Thus, we rule out the possibility of macroscopic phase separation into regions of different levels of Co intercalation, as has been suggested in other samples that have structural inhomogeneity (see the Appendix) [41].

Upon cooling, the ZF measurements show well-resolved oscillations, characteristic of long-range magnetic order [see Fig. 1(b)]. In principle, these data should be fitted with three parts: two arising from muons stopping in the sample (corresponding to muon-spin components perpendicular and parallel to the internal field) and one arising from muons stopping outside the sample. In practice, the part arising from the component of the muon spin parallel to the internal field is indistinguishable from the background contribution, and hence the data were fitted with a Lorentzian damped internal field function

$$A_{ZF}(t) = A[f_{osc}\cos(\gamma_\mu B_{int} t)\exp(-\Lambda t) + (1 - f_{osc})\exp(-\lambda t)], \quad (2)$$

where A is the initial asymmetry, f_{osc} is the oscillating fraction that arises from the component of muon spins inside the sample that are perpendicular to the internal magnetic field B_{int}, and $\gamma_\mu/(2\pi) = 135.5$ MHz/T is the gyromagnetic ratio of the muon. The depolarization rates Λ and λ characterize the damping of the oscillating and nonoscillating parts of the μSR signal, respectively. The damping Λ arises due to a distribution of magnetic fields at the muon site, predominantly arising from static disorder. The longitudinal relaxation rate λ reflects depolarization due to dynamic fluctuations. The temperature evolution of the fit parameters is shown in Figs. 1(c) and 1(d), and is typical for the onset of a second-order phase transition below $T_N = 168$ K. Figure 1(c) shows the gradual increase of the field at the muon site below T_N, which saturates at 66 mT. In contrast, the oscillating component of the phase fraction sharply increases below T_N, and remains constant until a slight upturn below 30 K (yellow shaded region), where the magnetization also exhibits a small kink [6]. This has previously been noted as the temperature where charge order in $Co_{1/4}NbSe_2$ occurs [28], or long-range magnetic order onsets for the $Co_{1/3}NbSe_2$ analog [41].

We describe the internal field with a power-law dependence

$$B = B_0(1 - (T/T_N)^\alpha)^\beta, \quad (3)$$

where B_0 is the internal field at zero temperature, α describes the scaling of low-energy excitations, and β is the critical exponent. We obtain $\alpha = 2.81(7)$ and $\beta = 0.351(8)$, with $B_0 = 66.0(2)$ mT and $T_N = 167.0(2)$ K. While the error on β makes it consistent with multiple spin types [$\beta = 0.365$ for three-dimensional (3D) Heisenberg spins and $\beta = 0.346$ for 3D XY-type spins], α is more informative. One expects $\alpha = 1.5$ for a ferromagnet and 2 for an antiferromagnet [44]; hence, our $\alpha > 2$ suggests that $Co_{1/4}NbSe_2$ is consistent with a magnetic order where moments are aligned antiparallel, plus gapped spin wave excitations [45].

The evolution of the muon spin relaxation rates Λ and λ is shown in Fig. 1(d). As can be seen, the dominant relaxation is due to static disorder, with Λ around 40 times greater than the dynamic λ. Below 30 K, there is a decrease in λ, with an increase in the amplitude of the oscillating (and hence static) signal despite no change in the overall magnetic volume fraction. We are in the slow fluctuation limit, where the spectra are dominated by the static response, and the rate of magnetic fluctuations ν is small compared to the static distribution of fields at the muon site. In this regime, $\lambda \propto \nu$. This indicates that at low T, we observe a slowing down of spin fluctuations and a more static magnetic response. We also observe that above T_N the λ rate falls to zero, which suggests the absence of precursor magnetic fluctuations on the μ^+SR timescale. Our results restrict any precursor fluctuations to be very roughly above $\simeq 10^{12}$ Hz, or slower than $\simeq 10^4$ Hz [45]. Therefore, if the origin of the persistent band splitting from the photoemission studies is dynamic, it must be caused by fluctuations that are faster than what can be observed in μ^+SR. Alternatively, surface states may contribute to the photoemission data, to which μ^+SR is not sensitive.

To further understand the μ^+SR spectra, we have computed the location of the muon stopping site in $Co_{1/4}NbSe_2$ using a DFT + μ approach [46] with MuFinder [47] (see the Appendix). We find a single site, shown in Fig. 1(a), located in the Nb layers, at the centers of Nb triangles adjacent to the Co site. This local symmetry matches the muon site in a sister material, $Cr_{1/3}NbS_2$ [38], therefore suggesting that the muon stopping site may be robust to changes in intercalation in this series. This muon stopping site can be understood by considerations of chemical bonding between the muon and the neighboring Nb (see the Appendix).

We have simulated the dipole field (note that the exchange-bias hyperfine field is zero by symmetry at this site) at the muon sites for various different magnetic structures and compared the results with ZF experimental data where the 45° spin rotation means that we are sensitive to the magnetic field at the muon site in both the *ab* plane (perpendicular, green) and along the *c* axis (parallel, orange) (Fig. 2). We find that a magnetic structure where moments are aligned antiparallel and along the *c* axis provides excellent agreement between our calculations and the experimental data, as shown in Fig. 2(a). This magnetic configuration is consistent with altermagnetism. The simulations suggest a magnetic moment of 1.610(4) μ_B/Co, only slightly higher than the ∼1.374(98) μ_B/Co reported in Ref. [6] from neutron scattering. Understanding the moment in intercalated TMDs is an ongoing challenge [48]; it has been suggested that the peculiar moment in $Co_{1/4}NbSe_2$ may be explained by the complex crystal field splitting arising due to the local Co symmetry [5]. Further, the simulations predict that around 20% of the muons are stopping in regions where there is no long-range order (e.g, in the sample holder), consistent with the fitting shown in Fig. 1(c). No other magnetic structure, such as one where the magnetic moments are pointing in the *ab* plane, is able to reproduce such a good match to the experimental data or theoretical predictions. For completeness, we show one such structure in Fig. 2(b), where the moments are aligned in the [210] plane, where the predicted moment is over 3 μ_B/Co.

Having understood the magnetic structure, we now turn to the effect of applying a magnetic field along the *c* axis.

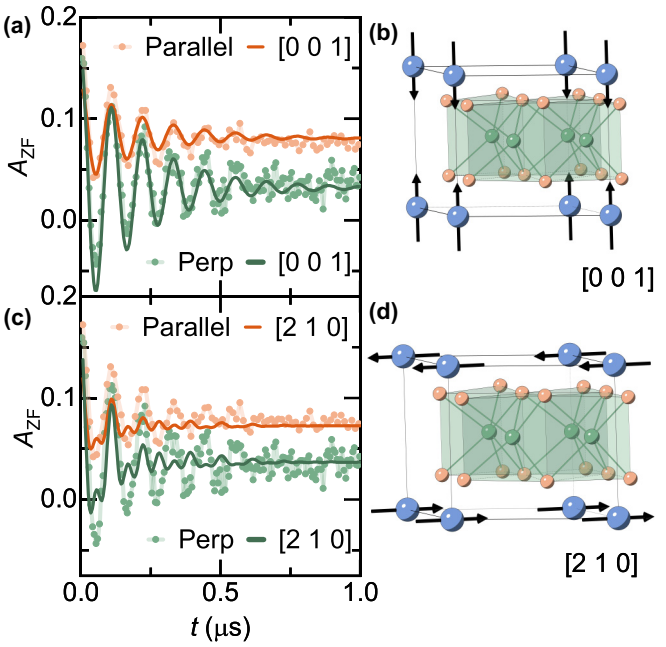


FIG. 2. Simulations of zero-field μ^+SR spectra for different magnetic structures. (a), (b) Simulations against ZF μ^+SR spectra and schematic of structure for the accepted magnetic structure of $Co_{1/4}NbSe_2$, moments aligned antiparallel along the c axis. (c), (d) Simulations against ZF μ^+SR spectra and schematic of structure for moments aligned in the [210] plane. In panels (b) and (d), the atoms are Co (blue), Nb (green), and Se (peach). Zero-field μ^+SR spectra extracted from two detector pairs—forward-backward (parallel) and up-down (perpendicular)—are shown.

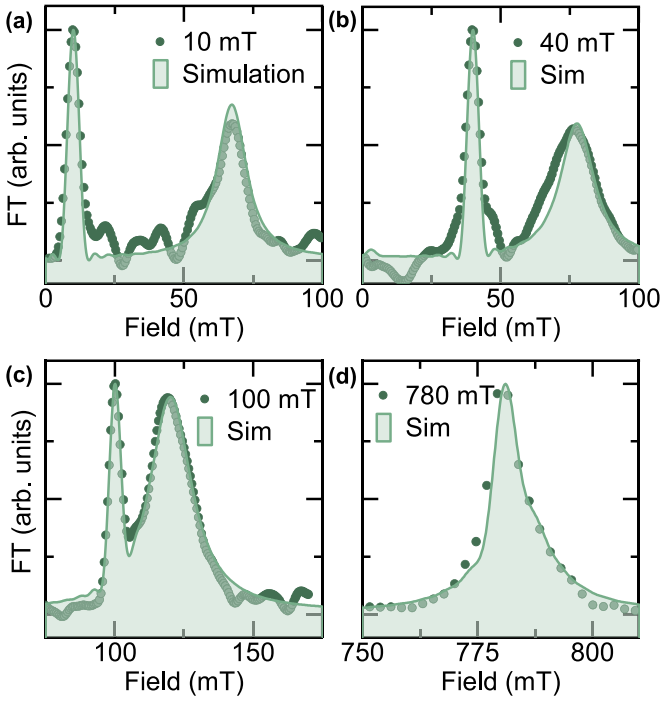


FIG. 3. Experimental and simulated TF-μ^+SR data. Comparison of experimental (dark green points) and simulated (light green shaded area) μ^+SR data at 5 K under applied transverse fields of (a) 10 mT, (b) 40 mT, (c) 100 mT, and (d) 780 mT.

We have performed transverse-field (TF) μ^+SR experiments, where we are sensitive to the precession of the muon spin in the vector sum of the internal and applied fields. Adding the relevant applied field to our calculated internal field for the c-axis-aligned magnetic structure, we obtain predictions for the TF μ^+SR spectra, which we compare to the experimental measurements in Fig. 3. Once again we obtain an excellent agreement by only slightly decreasing the background contribution at higher fields (which is expected experimentally due to beam focusing) and slightly changing the phenomenological damping factor (this effect is consistent with no change to the magnetic structure; see the Appendix). We have thus demonstrated that no modification to the magnetic structure is needed to explain the μ^+SR spectra up to 0.78 T. The field dependence of the magnetization in $Co_{1/4}NbSe_2$ [6] is linear between 0 and 5 T; thus, as μ^+SR rules out any changes in the magnetic structure between 0 and 0.78 T, we conclude that the magnetic configuration is robust under c-axis-aligned applied fields of at least 5 T. We note the same conclusion is reached with model-independent analysis (see the Appendix).

Finally, we return to the low-temperature change in the μ^+SR spectra, which coincides with a kink in magnetic susceptibility (see the Appendix). Having ruled out the possibility of macroscopic phase separation on the basis of our weak-transverse-field measurements, and additional dipole-field simulations (see the Appendix), the origin of this feature must be intrinsic to $Co_{1/4}NbSe_2$. One explanation could involve nanoscale regions, possibly centered around extra Co inclusions, that remain dynamically fluctuating and disordered until lower temperatures. As these regions undergo ordering, the average field at the muon site would remain largely unchanged, as observed in Fig. 1(c). This transition would lead to a reduction in the dynamic response [λ in Fig. 1(d)], accompanied by an increase in the width of the field distribution at the muon site [Λ in Fig. 1(d)], due to the different symmetry of these Co inclusions. Alternatively, the characteristic temperature of 30 K coincides with the CDW transition temperature of $NbSe_2$. If local structural distortions occur within the $NbSe_2$ layers below 30 K due to the onset of the CDW, these distortions could modify the bonding environment, thereby affecting the exchange coupling between Co inclusions. Such an effect could lead to a local pinning of magnetic fluctuations by the CDW-induced lattice distortions, potentially influencing the observed magnetic dynamics. This interplay between CDW order and local magnetic fluctuations would suggest a possible coupling between the electronic and magnetic degrees of freedom, warranting further investigation through complementary techniques such as x-ray diffraction (XRD) and Raman spectroscopy to directly probe the structural modifications and their impact on magnetic order.

III. SUMMARY

In this study, we employed the highly sensitive local magnetic technique μ^+SR, combined with muon stopping site calculations, to evaluate the homogeneity of the magnetic state, determine the magnetic volume fraction, differentiate

between a canted antiferromagnetic configuration and one with spins strictly aligned along the c axis, and probe slow precursor magnetic fluctuations in the normal state of $Co_{1/4}NbSe_2$. Our findings reveal a sharp second-order phase transition to a c-axis, full-volume-fraction, homogeneous magnetic order below $T_N = 168$ K. The magnetic structure comprises moments aligned antiparallel along the c axis, which is consistent with the previous neutron scattering experiment, as required for the emergence of altermagnetism. Additionally, we find no evidence of precursor slow magnetic fluctuations above $T_N = 168$ K within the time resolution of μ^+SR. This indicates that the persistent spin splitting above the ordering temperature is not caused by slow fluctuations occurring on the megahertz scale. Furthermore, we demonstrate that the width of the distribution of the fields at the muon site has a very weak dependence on the applied field. This highlights the robustness of the magnetic state in $Co_{1/4}NbSe_2$ up to an applied field of 0.78 T (and probably 5 T) when applied along the c axis, as suggested by magnetization experiments. This robust behavior is important both for the opportunity to employ other experimental probes that require large applied fields and for potential spintronic applications.

Having established a robust magnetic state in $Co_{1/4}NbSe_2$, several important questions remain that are to be addressed in future studies. A key manifestation of altermagnetism is its potential to exhibit an anomalous Hall effect (AHE). In $Co_{1/4}NbSe_2$, the AHE is only expected when the easy axis lies within the *ab* plane and is perpendicular to the Co–Co bond [6]. As these conditions are not met, no AHE will be observed. However, the strong experimental evidence supporting altermagnetism in this material motivates future investigations aimed at tuning the magnetic structure through uniaxial strain, hydrostatic pressure, high magnetic fields, and other external stimuli. Such tuning could induce a transition from an out-of-plane to an in-plane configuration, thereby realizing AHE. If achieved, this would provide a comprehensive demonstration of altermagnetic properties, further solidifying the system's potential for spintronic applications. Moreover, this tunability presents an opportunity to explore phonon-magnon coupling—specifically, how atomic displacements influence exchange interactions, and how magnetism affects lattice dynamics.

Beyond $Co_{1/4}NbSe_2$, remains the opportunity to exercise further control of the magnetic properties of TMDs via tuning of the intercalant. As has been shown for Co-intercalated $NbSe_2$, slight changes in the stoichiometry of the Co can dramatically change the physical properties of the system [41]. This idea may be extended to include the vast number of combinations between TMDs and intercalants of different varieties such as transition-metal ions, organic linkers, and alkali metals [15–19,31,32]. Addressing these fundamental aspects would provide deeper insights into the intrinsic interactions governing altermagnetic materials, potentially revealing couplings relevant to quantum materials and next-generation electronic devices.

ACKNOWLEDGMENTS

The μSR experiments were carried out at the Swiss Muon Source (SμS), Paul Scherrer Insitute, Villigen, Switzerland. Z.G. acknowledges support from the Swiss National Science Foundation (SNSF) through SNSF Starting Grant (No. TMSGI2_211750). N.J.G. and I.M. were supported by the Army Research Office under Cooperative Agreement No. W911NF-22-2-0173.

Z.G. supervised the project and, together with M.J., conceived the study. Crystal growth: R.B.R. and N.J.G. μSR experiments, analysis, and corresponding discussions: J.N.G., T.J.H., M.J., H.L., and Z.G. Muon stopping site calculations: T.J.H. and I.M. Local field analysis: T.J.H.. Figure development and writing of the paper: J.N.G., T.J.H., and Z.G. with contributions from all authors. All authors discussed the results, interpretation, and conclusion.

The authors declare no financial/commercial conflict of interest.

DATA AVAILABILITY

The data are not publicly available. The data are available from the authors upon reasonable request.

APPENDIX

1. Experimental details

Muon spin rotation measurements of $Co_{1/4}NbSe_2$ were performed on the GPS instrument [42] at the Swiss Muon Source, Paul Scherrer Institute, Villigen, Switzerland. Single-crystal samples were placed in a mosaic arrangement (i.e., the c axis was aligned, without alignment in the *ab* plane), and the muon spin was rotated to 45° so that measurements were sensitive to both the *ab* plane and c axis. We extracted zero-field μ^+SR spectra from two detector pairs—forward-backward (referred to as the parallel component) and up-down (referred to as the perpendicular component)—as shown in the main text. We used single crystals with a thickness of 0.3 mm. As the sample was relatively thin, some muons passed straight through. The sample is mounted on a copper fork using Mylar tape (a polyester film with a thin vacuum-deposited aluminum layer), in which a fraction of the implanted muons come to rest. In addition, a small number of muons stop in the cryostat walls. All of these contributions are approximately temperature independent over the investigated temperature range and therefore give rise to a constant background signal of approximately 17%. The resulting background of 17% was accurately determined from weak transverse-field μSR measurements. These measurements are summarized in Fig. 4, which shows the μSR spectra recorded under a field of 3 mT at 200 and 5 K [Fig. 4(a)], as well as the temperature dependence of the amplitude [Fig. 4(b)]. From the absolute value of the amplitude, the background fraction was estimated, and the relaxation rate of the spectra at 5 K shows that any relaxation of the polarization of muons stopping in the background is $\leqslant 0.05$ μs^{-1}. This low value suggests that most of the background muons stop in the tape, which is known to have a very small, temperature-independent relaxation rate. A continuous-flow cryostat was used to control the temperature across a range of 5–300 K. Measurements were conducted in zero field, and transverse-fields between 3 mT and 0.78 T. Data were analyzed using the MUSRFIT software [49].

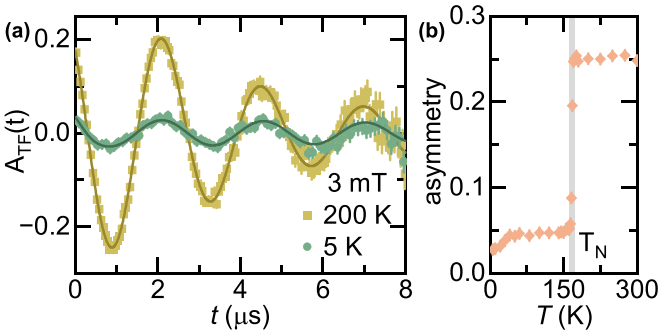


FIG. 4. Weak-transverse field μ^+SR measurements of $Co_{1/4}NbSe_2$. (a) Weak-transverse-field spectra measured at 5 and 200 K in an applied field of 3 mT. The difference in magnitude of the oscillation reflects the increase in magnetic volume fraction at low temperatures. (b) Temperature evolution of asymmetry, which directly reflects the magnetic volume fraction.

The muon stopping sites in $Co_{1/4}NbSe_2$ were calculated using a DFT + μ approach [46] using the MuFinder application [47]. Density functional theory calculations were performed using the plane-wave pseudopotential code CASTEP [50]. The PBEsol functional [51] was used in all calculations. Calculations were converged to 2.5 meV/atom using a plane-wave cutoff of 600 eV and a $3 \times 3 \times 3$ k-point grid [52]. Thirty-six random positions were initialized in the conventional unit cell ($\sim 7 \times 7 \times 12$ Å). The atomic positions were subsequently allowed to relax until the energy and atomic positions have converged to better than 1×10^{-3} meV/atom and 1×10^{-4} Å, respectively, and the maximum force on any atom is less than 2×10^{-3} eV/Å. The final muon positions are clustered using the MuFinder application to give the candidate muon stopping sites; each cluster was subsequently used to initialize a calculation in a $2 \times 2 \times 1$ supercell ($\sim 14 \times 14 \times 12$ Å) to ensure that the muons did not self-interact. The final muon stopping site was used in the MUESR code [53] to calculate the dipolar field at these sites for candidate magnetic structures. We have accounted for the sample orientation (a mosaic of crystals aligned along the c axis, with no alignment in the ab plane, see below for details), which means we can simultaneously predict the time-dependent spin polarization in two different detector pairs directly from the calculated vector field at the muon site. This has the advantage of giving sensitivity to internal field directions, as well as magnitudes, which further helps compare different potential magnetic structures. In our simulations, we assume a fraction of the muons stop outside of the sample and apply a phenomenological damping factor to account for the distribution of fields at the muon site that likely arises due to the finite magnetic domain size. Finally, we allow the nonprecessing component of the signal to weakly relax, accounting for any dynamics in the material.

2. Determination of the muon stopping site in $Co_{1/4}NbSe_2$

Our DFT calculations reveal four potential stopping sites, given in Table I. The lowest-energy site causes almost no distortion to the crystal structure; however, the higher-energy sites are slightly more disruptive and significantly higher in energy, suggesting that they are less likely to be occupied.

TABLE I. The calculated muon stopping sites in $Co_{1/4}NbSe_2$. Energies are given with respect to the lowest-energy site, which is believed to be the only one occupied. Coordinates are fractional coordinates in the conventional unit cell.

Site	Energy (eV)	Coordinates	Wyckoff site
1	0	(0.83, 0.66, 0.25)	6*h*
2	1.04	(0.53, 0.06, 0.10)	12*k*
3	1.37	(0.27, 0.13, 0.01)	12*k*
4	1.58	(0.18, 0.09, 0.09)	12*k*

Although the crucial parameter for determining occupation is the energy barrier between sites, rather than the energy of the local minima that are individual stopping sites, it would be surprising for sites 2–4, where the local minima is over 1 eV higher in energy, to be occupied. Irrespective of the choice of magnetic structure, when simulating the field at the different muon sites, we find that the field at sites 3 and 4 (situated near Co atoms) is implausibly high, and thus can independently be assumed to be unoccupied. The experimental ZF μ^+SR spectra presented in the main text show the same, single frequency in both detector pairs, further suggesting only a single muon stopping site. Most significantly, our excellent agreement between the calculations and experimental data is achieved with 100% occupation of the lowest-energy muon site; we therefore conclude that this is the only occupied site in experiment.

3. Derivation of the μ^+SR response to a partially orientated mosaic of crystals

In μ^+SR experiments, one is often able to align a single crystal axis, with no knowledge of the alignment in the other directions. As such, it is useful to explicitly derive the μ^+SR response to such a partially orientated mosaic of single crystals. We start with the general vector form of the time-dependent polarization $\boldsymbol{P}(t)$ arising from a muon stopping in a single internal field $\boldsymbol{B}_\mu$ [54]

$$\boldsymbol{P}(t) = [\boldsymbol{P}(0)\cdot\hat{\boldsymbol{b}}_\mu]\hat{\boldsymbol{b}}_\mu + \{\hat{\boldsymbol{b}}_\mu \times [\boldsymbol{P}(0)\times\hat{\boldsymbol{b}}_\mu]\}\cos(\gamma_\mu B_\mu t) + [\boldsymbol{P}(0)\times\hat{\boldsymbol{b}}_\mu]\sin(\gamma_\mu B_\mu t), \tag{A1}$$

where $\boldsymbol{P}(0)$ is the initial polarization of the muon spin (assumed to be a unit vector), $\hat{\boldsymbol{b}}_\mu = \boldsymbol{B}_\mu/|\boldsymbol{B}_\mu| = \boldsymbol{B}_\mu/B_\mu$, and $\gamma_\mu = 2\pi \times 135.538\,810(3)$ MHz/T is the gyromagnetic ratio of the muon. Typically, the initial spin polarization is taken to be along $\hat{\boldsymbol{z}}$; however, we employ a different convention, where the aligned sample axis is along $\hat{\boldsymbol{z}}$, with the initial spin polarization set with respect to this. Further, it is helpful to recast our problem in spherical polar coordinates, i.e., $\hat{\boldsymbol{b}}_\mu = (\sin\theta\cos\phi, \sin\theta\sin\phi, \cos\theta)$.

From this equation, one is able to perform various averages. The most familiar is the powder average, assuming a completely unoriented sample:

$$\boldsymbol{P}_{\text{powder}}(t) = \frac{1}{4\pi}\int_{\theta=0}^{\theta=\pi}\int_{\phi=0}^{\phi=2\pi}\boldsymbol{P}(t)\sin\theta\,\mathrm{d}\phi\,\mathrm{d}\theta. \tag{A2}$$

Taking $\boldsymbol{P}(0) = (1/\sqrt{2}, 0, 1/\sqrt{2})$, which corresponds to the experimental setup used in this paper, specifically a spin rotation of 45° away from the incoming muon-momentum direction, we gain the expected result

$$\boldsymbol{P}_{\text{powder}}(t) = \begin{pmatrix} \frac{1+2\cos(\gamma_\mu B_\mu t)}{3\sqrt{2}} \\ 0 \\ \frac{1+2\cos(\gamma_\mu B_\mu t)}{3\sqrt{2}} \end{pmatrix}, \tag{A3}$$

i.e., the same signal in two perpendicular directions (corresponding the the forward-backward and up-down detector pairs) with an appropriate weighting, and no signal in the third direction. Similarly, the relevant integral for the partially aligned mosaic is

$$\boldsymbol{P}_{\text{mosaic}}(t) = \frac{1}{2\pi}\int_{\phi=0}^{\phi=2\pi} \boldsymbol{P}(t)\,\mathrm{d}\phi, \tag{A4}$$

which gives, using the same $\boldsymbol{P}(0)$,

$$\boldsymbol{P}_{\text{mosaic}}(t) = \begin{pmatrix} \frac{(3+\cos 2\theta)\cos(\gamma_\mu B_\mu t)+2\sin^2\theta}{4\sqrt{2}} \\ -\frac{\cos\theta\sin(\gamma_\mu B_\mu t)}{\sqrt{2}} \\ \frac{\cos^2\theta+\sin^2\theta\cos(\gamma_\mu B_\mu t)}{\sqrt{2}} \end{pmatrix}. \tag{A5}$$

This gives the surprising result that there should be a time-dependent polarization in all three directions, which one will not observe experimentally. To account for this, we must also consider alignment of the sample under the transformation $\hat{z} \mapsto -\hat{z}$, which produces the same result as Eq. (A5), but with the second component multiplied by -1. Averaging over these two results gives our final result

$$\boldsymbol{P}_{\text{mosaic}}(t) = \begin{pmatrix} \frac{(3+\cos 2\theta)\cos(\gamma_\mu B_\mu t)+2\sin^2\theta}{4\sqrt{2}} \\ 0 \\ \frac{\cos^2\theta+\sin^2\theta\cos(\gamma_\mu B_\mu t)}{\sqrt{2}} \end{pmatrix}. \tag{A6}$$

4. Simulations of the field at the muon site in $Co_{1/3}NbSe_2$

One suggestion [41] for the observed low-T changes in the ZF μ^+SR spectra is that a small fraction of the sample is actually closer to $Co_{1/3}NbSe_2$, leading to spatially separated magnetic domains at low-T when these regions magnetically order. To explore this possibility, we have calculated the field at the muon site in $Co_{1/3}NbSe_2$, assuming the proposed helical structure [41], which predicts a helix with $\boldsymbol{q} = (0, 1/3, 0.048)$, and assume the same magnetic moment as found in the main text, specifically 1.61 μ_B/Co. We follow the same approach as set out for $Co_{1/4}NbSe_2$. However, as the structure is incommensurate, the fields at the muon site are calculated many times, with the initial phase of the magnetic structure varied continuously; this captures the effect of muons stopping in all different unit cells. We have assumed that the muon site is the same as that found for isostructural $Cr_{1/3}NbS_2$ [38] (which shares the same local symmetry as the muon site in $Co_{1/4}NbSe_2$), as is often the case for structurally similar compounds [55]. As is typical in materials with a helical magnetic structure, the internal field distribution seen by μ^+SR comprises two peaks (centered around 20 and 85 mT) with a continuous distribution between them, as shown in Fig. 5. As can be seen, the two peak fields are higher and lower than the experimentally measured internal field. These features would be very obvious in the experimental data (even at a small sample volume); therefore, as we do not observe these features, we conclude that this is unlikely to be an explanation for the low-T changes in the asymmetry spectra.

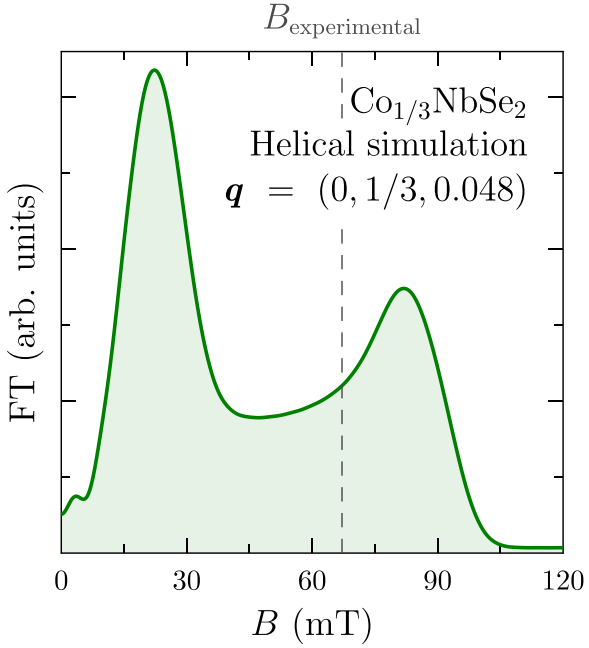


FIG. 5. Simulated field at the muon site in $Co_{1/3}NbSe_2$. The field measured experimentally in this work at 5 K is also indicated.

5. Robustness of magnetic state with applied field

Transverse-field μ^+SR data were fit with the following equation:

$$A_{\text{TF}}(t) = \sum_i A_i \exp(-\sigma_i t)\cos(\gamma_\mu B_i t + \varphi_i), \tag{A7}$$

where A_i is the asymmetry, σ_i is the relaxation rate, γ_μ is the gyromagnetic ratio of the muon, B_i is the magnetic field, and φ_i is the phase shift. Two components were used for all fits, one accounting for the applied field (B_{appl}) and one for the internal field of the sample (B_{int}). Zero-field data at 5 K were checked against this model and gave consistent results.

To further verify the field independence of the magnetic structure, we can consider the expected scaling of experimentally measured parameters in our TF μ^+SR measurements, providing a muon-site-independent verification of our results. The two parameters we consider are the difference between the measured internal field B_{int} and the externally applied field B_{appl} [Fig. 6(a)], and the associated damping σ [Fig. 6(b)]. We employ a toy model where we assume that the ZF magnetic structure (and hence contribution to the μ^+SR spectra from the magnetic structure) is field independent. Our ZF μ^+SR results reveal that $c = B_{\text{int}}(B_{\text{appl}} = 0)$ is perpendicular to the direction in which we apply B_{appl}; hence, in the TF μ^+SR measurements, $B_{\text{int}} = |\boldsymbol{B}_{\text{int}}| = \sqrt{B_{\text{int,ZF}}^2 + B_{\text{appl}}^2}$. Taking

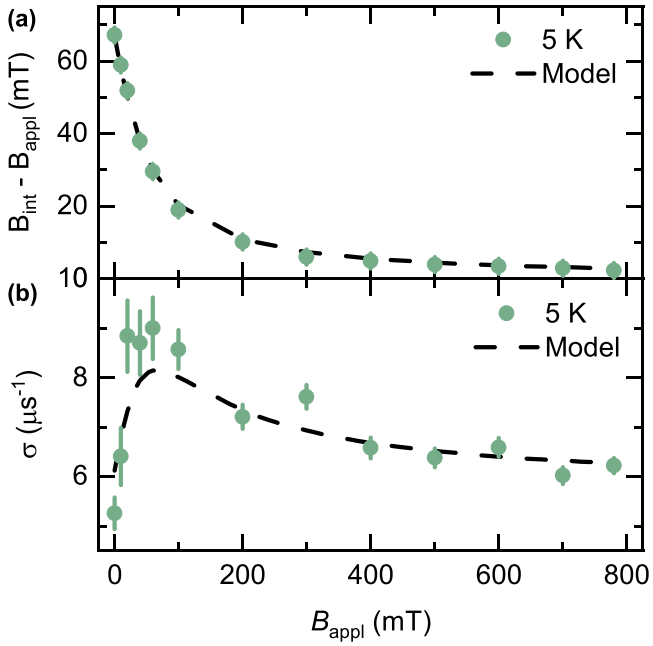


FIG. 6. Results from TF μ^+SR. The extracted parameters from fitting of TF μ^+SR are shown. The dashed line in both plots represents the muon-site-agnostic toy model detailed in the text, demonstrating that no modifications to the magnetic structure are needed to explain the spectra.

this form using $B_{\mathrm{int,ZF}}$ from the ZF μ^+SR measurements, and subtracting B_{appl}, gives the dashed line in Fig. 6(a), which well matches the experimental data.

To model σ, which is proportional to the width of the distribution of fields at the muon site, we assume a 3D normal distribution of fields (although we note we are only sensitive to two of these three directions) that is once again unchanged upon application of the applied field. Taking the standard definition $\sigma^2 = \frac{\gamma_\mu^2}{2}\langle(B - \langle B\rangle)^2\rangle$ [45], where $\langle\cdots\rangle$ represents an average, we can approximate

$$\sigma^2 \simeq \frac{\gamma_\mu^2}{2}\Big[\sqrt{(B_{\mathrm{int,ZF}} + \Delta B_{\mathrm{int,ZF}})^2 + (B_{\mathrm{appl}} + \Delta B_{\mathrm{int,ZF}})^2} - \sqrt{B_{\mathrm{int,ZF}}^2 + B_{\mathrm{appl}}^2}\Big], \tag{A8}$$

where $\Delta B_{\mathrm{int,ZF}}$ is the width of the distribution of fields, which we assume to be the same in all directions. Once again using $B_{\mathrm{int,ZF}}$ as determined from ZF μ^+SR measurements, we can well describe the data when $\Delta B_{\mathrm{int,ZF}} \simeq 95$ mT, as shown by the dashed line in Fig. 6(b). We note that in this scenario, with the average internal field perpendicular to the applied field, when $B_{\mathrm{appl}} = 0$, $\sigma \simeq \gamma_\mu \Delta B_{\mathrm{int,ZF},x}/\sqrt{2}$, and when $B_{\mathrm{appl}} \to \infty$, $\sigma \simeq \gamma_\mu \Delta B_{\mathrm{int,ZF},z}/\sqrt{2}$, where $\Delta B_{\mathrm{int,ZF},x}$ and $\Delta B_{\mathrm{ext,ZF},z}$ are the distribution widths in the internal field and external field direction, respectively. Further, the maximum in σ occurs when $B_{\mathrm{int,ZF}} = B_{\mathrm{appl}}$. Hence, without assuming any knowledge of the muon stopping site, we have demonstrated that no modifications to the magnetic structure are required to describe the TF μ^+SR data, and hence that the magnetic structure is robust up to at least 0.78 T.

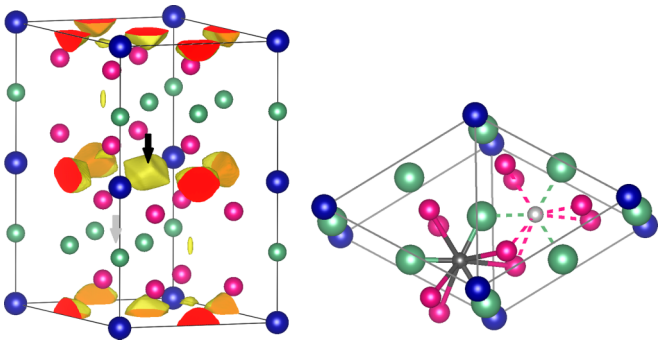


FIG. 7. Left: Electrostatic potential. The black arrow shows the location of the minimal potential, whereas the gray arrow shows the actual calculated stopping site. Nb is shown in green, Se in red, and Co in blue. Right: The calculated stopping site (black) vs an alternative site (which has a higher energy) with the same μ^+-Nb and μ^+-Se coordination.

6. Additional notes on the stopping sites in $Co_{1/4}NbSe_2$

In recent years, accurately calculating the muon stopping site has become routinely possible using the DFT + μ method [46] (where the muon is treated as a reduced mass proton) using applications such as MuFinder [47]. This method, while considerably more accurate than previous approaches, has made it harder to have good intuition about the stopping site. In contrast, an older, often inaccurate method, where the muon was assumed to stop at the electrostatic potential minimum with no distortion to the surrounding lattice, was easier to predict "by eye." In this Appendix, we provide some additional insights into the muon stopping site in $Co_{1/4}NbSe_2$, which may provide improved intuition in other materials.

If one calculates the electrostatic potential in $Co_{1/4}NbSe_2$, one finds that the minimum of the Coulomb potential occurs in the Co plane, due to the effect of the positive charge of Nb. This is shown in Fig. 7. An intuitive picture is therefore that the positively charged muon is attracted to this position, where it then tries to bond with the nearest ligand, stopping at a low-symmetry site. Conversely, our muon site is actually a high-symmetry position (as is often found in metals, for example, Cu [56]), in the Nb plane. This site, which does not have the z coordinate fixed by symmetry, is found to be exactly in the plane within computational accuracy; this means that the contact hyperfine coupling is zero by symmetry, and only the dipole contribution remains. To gain an intuitive understanding, we therefore must pose two questions: (1) Why does the muon prefer to stop inside the Nb plane, despite a higher electrostatic potential? (2) Why of the two equivalent (apart from Co) positions in the Nb plane does the muon prefer the one that is closer to Co?

To answer question (1), we have calculated the charge distribution, as shown in Fig. 8. This charge distribution suggests that there is a chemical bond between the μ^+ and the neighboring Nb atoms, which is of similar strength to the Nb–Se bond. Thus, in this compound the location of the stopping site is primarily determined not by electrostatic energy, but by chemical bonding.

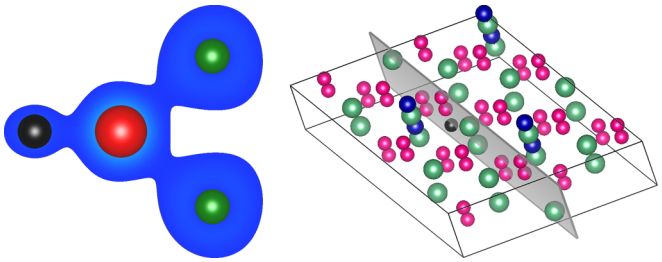


FIG. 8. Charge density isosurfaces (at $n = 0.05$ e/Å^3). On the left is a cut that is shown in the full cell on the right. The muon is shown in black, with the Nb in red, Se in green, and Co in blue.

Now considering question (2), we show in Fig. 7 two potential stopping sites inside the Nb plane. The realized site is in a region of higher electrostatic potential when compared to the unoccupied position, albeit not by much. One can again understand this by considering the chemical bonding between the μ^+ and the surrounding Nb. The length of the bonds that the μ^+ forms with Nb (solid tubes in Fig. 7) is about 0.1 Å shorter than the dashed lines for the hypothetical alternative site; thus, this bond is stronger, resulting in this site being occupied in preference to the alternative possibility. Thus, the muon position in $Co_{1/4}NbSe_2$ can be intuitively understood by considering the chemistry of the system, with the electrostatic potential not playing an important role.

7. Structural and physical characterization of $Co_{1/4}NbSe_2$

In the following, we present the structural and physical characterization of the $Co_{1/4}NbSe_2$ crystal studied in this work. Using energy-dispersive x-ray spectroscopy on a Bruker FEI Magellan instrument operated at 20 keV, the elemental composition of Co:Nb:Se was determined to be 0.28:1:2, with an estimated uncertainty of approximately 3%–5% [6] and electron diffraction patterns [Figs. 9(a) and 9(b)] confirm that the material retains a well-ordered 1/4 intercalated structure. The present $Co_{1/4}NbSe_2$ crystals originate from the same batch reported by Regmi *et al.* [6] and display identical structural, magnetic, and transport properties (Figs. 9 and 10). Minor deviations in Co intercalation levels, however, may slightly modify the magnetic susceptibility and introduce disorder. Our samples exhibit a well-defined 2×2 superlattice, as verified by both single-crystal XRD [6] and electron diffraction imaging. Notably, even at the $Co_{0.28}NbSe_2$ composition, the ordered 1/4 intercalated phase stabilizes an A-type antiferromagnetic arrangement that enables altermagnetism [5]. By contrast, Mandujano *et al.* [41] reported that in $Co_{0.28\pm\delta}NbSe_2$, structural disorder can lead to the coexistence of both $2 \times 2a$ and $\sqrt{3} \times \sqrt{3}a$ configurations, corresponding to commensurate and incommensurate *A*-type antiferromagnetic states, as revealed by single-crystal precession imaging. Such disorder is absent in our crystals, as evidenced by the sharp electron diffraction patterns shown in Figs. 9(a) and 9(b) and the atomic-scale structural analysis in Fig. 10.

In addition, the absence of the 30 K anomaly in the resistivity and magnetization measurements, which probe

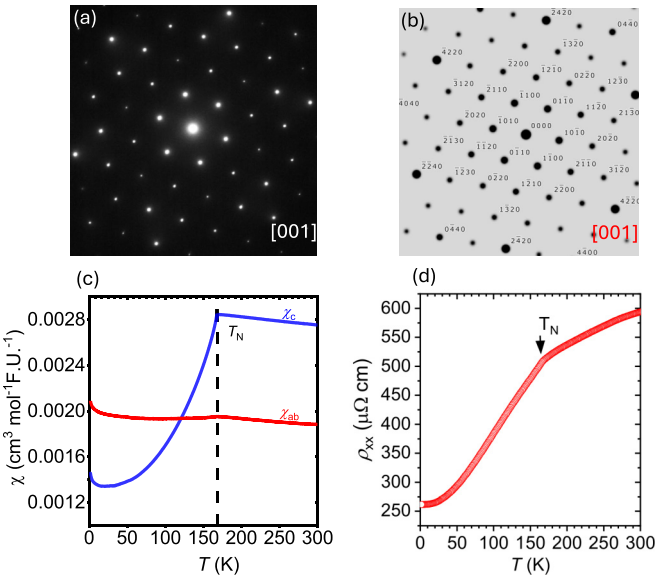


FIG. 9. Structural and physical characterization. (a) The electron diffraction pattern for $Co_{1/4}NbSe_2$ as shown along the [001] zone axis. (b) Simulated electron diffraction pattern. (c) The temperature dependence of magnetic susceptibility for $Co_{1/4}NbSe_2$ measured for the magnetic fields applied within the *ab* plane and along the *c* axis. There is no kink at 30 K, highlighting no bulk magnetic transition or inhomogeneity of the sample. (d) The temperature dependence of resistivity for $Co_{1/4}NbSe_2$.

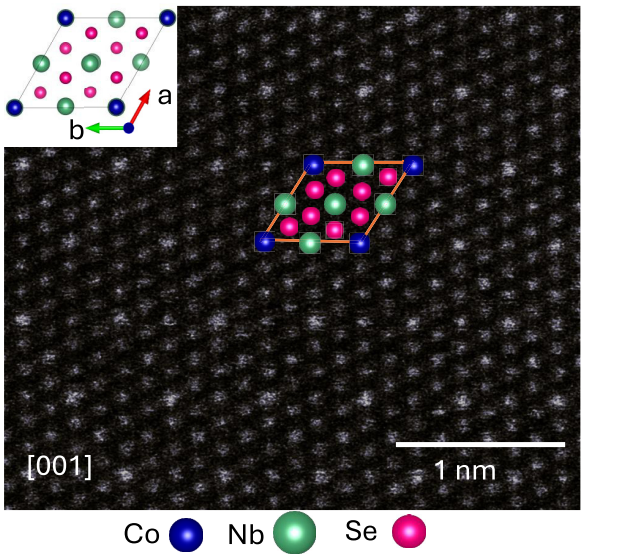


FIG. 10. Atomic structural analysis of $Co_{1/4}NbSe_2$. The structure of $Co_{1/4}NbSe_2$ is precisely characterized by atomic-scale structural analysis using aberration-corrected high-angle annular dark field scanning transmission electron microscopy imaging along the [001] direction. This approach reveals a distinct 2×2 periodic arrangement of Co atoms, forming a superstructure relative to the $NbSe_2$ unit cell. Inset shows the structure of $Co_{1/4}NbSe_2$ along the crystallographic *c* axis from VESTA. The unit cell is consistent with Co adopting a one-quarter occupancy pattern, intercalated between $NbSe_2$ layers.

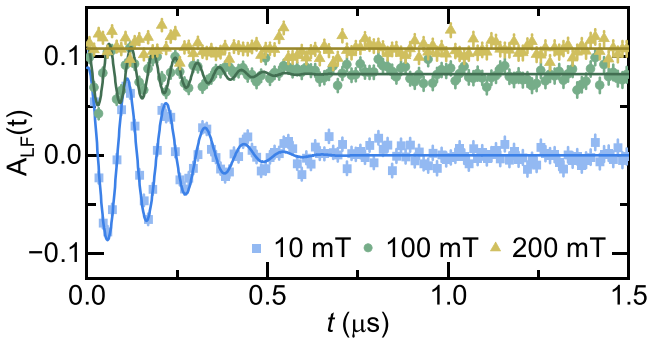


FIG. 11. Longitudinal-field μ^+SR measurements of $Co_{1/4}NbSe_2$. Longitudinal-field μ^+SR spectra measured at 5 K in various fields up to 200 mT. The muon is completely decoupled from the internal field by 200 mT, indicating static relaxation. α has been fixed across the different fields.

macroscopic properties, indicates the high quality of our crystals and the absence of any impurity phase. In contrast, μ^+SR is an extremely sensitive local probe that can detect even very subtle changes in the magnetic environment at the microscopic level. The fact that no anomaly is observed in macroscopic characterization techniques, while a weak feature is detected by μ^+SR (see the main text), suggests that only minor changes occur on the microscopic scale, which remain below the sensitivity of bulk probes.

8. Longitudinal-field μ^+SR results

Figure 11 shows the μ^+SR spectra measured in a magnetic field applied longitudinal to the muon spin polarization. With increasing field, the depolarization is progressively suppressed, and full decoupling is achieved at a field approximately three times larger than the internal field, indicating that the magnetism in $Co_{1/4}NbSe_2$ is predominantly static. This exactly matches our results in the main text where we conclude that the system is dominated by the static response as we are in the slow fluctuation regime.

[1] L. Šmejkal, J. Sinova, and T. Jungwirth, Beyond conventional ferromagnetism and antiferromagnetism: A phase with nonrelativistic spin and crystal rotation symmetry, Phys. Rev. X **12**, 031042 (2022).

[2] L. Šmejkal, J. Sinova, and T. Jungwirth, Emerging research landscape of altermagnetism, Phys. Rev. X **12**, 040501 (2022).

[3] I. Mazin (The PRX Editors), Editorial: Altermagnetism—A new punch line of fundamental magnetism, Phys. Rev. X **12**, 040002 (2022).

[4] I. I. Mazin, K. Koepernik, M. D. Johannes, R. González-Hernández, and L. Šmejkal, Prediction of unconventional magnetism in doped $FeSb_2$, Proc. Natl. Acad. Sci. USA **118**, e2108924118 (2021).

[5] N. Dale, O. A. Ashour, M. Vila, R. B. Regmi, J. Fox, C. W. Johnson, A. Fedorov, A. Stibor, N. J. Ghimire, and S. M. Griffin, Non-relativistic spin splitting above and below the Fermi level in a g-wave altermagnet, arXiv:2411.18761.

[6] R. B. Regmi, H. Bhandari, B. Thapa, Y. Hao, N. Sharma, J. McKenzie, X. Chen, A. Nayak, M. E. Gazzah, B. G. Márkus, L. Forró, X. Liu, H. Cao, J. F. Mitchell, I. I. Mazin, and N. J. Ghimire, Altermagnetism in the layered intercalated transition metal dichalcogenide $CoNb_4Se_8$, Nat. commun. **16**, 4399 (2025).

[7] C.-C. Wei, E. Lawrence, A. Tran, and H. Ji, Crystal chemistry and design principles of altermagnets, ACS Org. Inorg. Au **4**, 604 (2024).

[8] S. S. Fender, O. Gonzalez, and D. K. Bediako, Altermagnetism: A chemical perspective, J. Am. Chem. Soc. **147**, 2257 (2025).

[9] L. Han, X. Fu, R. Peng, X. Cheng, J. Dai, L. Liu, Y. Li, Y. Zhang, W. Zhu, H. Bai, Y. Zhou, S. Liang, C. Chen, Q. Wang, X. Chen, L. Yang, Y. Zhang, C. Song, J. Liu, and F. Pan, Electrical 180° switching of Néel vector in spin-splitting antiferromagnet, Sci. Adv. **10**, eadn0479 (2024).

[10] Z. Zhou, X. Cheng, M. Hu, R. Chu, H. Bai, L. Han, J. Liu, F. Pan, and C. Song, Manipulation of the altermagnetic order in CrSb via crystal symmetry, Nature (London) **638**, 645 (2025).

[11] J. Ding, Z. Jiang, X. Chen, Z. Tao, Z. Liu, T. Li, J. Liu, J. Sun, J. Cheng, J. Liu, *et al.*, Large band splitting in *g*-wave altermagnet CrSb, Phys. Rev. Lett. **133**, 206401 (2024).

[12] G. Yang, Z. Li, S. Yang, J. Li, H. Zheng, W. Zhu, Z. Pan, Y. Xu, S. Cao, W. Zhao, *et al.*, Three-dimensional mapping of the altermagnetic spin splitting in CrSb, Nat. Commun. **16**, 1442 (2025).

[13] I. I. Mazin, Altermagnetism in MnTe: Origin, predicted manifestations, and routes to detwinning, Phys. Rev. B **107**, L100418 (2023).

[14] D. Jost, R. B. Regmi, S. Sahel-Schackis, M. Scheufele, M. Neuhaus, R. Nickel, F. Yakhou, K. Kummer, N. Brookes, L. Shen, G. L. Dakovski, N. J. Ghimire, S. Geprägs, and M. F. Kling, Chiral altermagnon in MnTe, arXiv:2501.17380.

[15] J. A. Wilson and A. Yoffe, The transition metal dichalcogenides discussion and interpretation of the observed optical, electrical and structural properties, Adv. Phys. **18**, 193 (1969).

[16] Q. H. Wang, K. Kalantar-Zadeh, A. Kis, J. N. Coleman, and M. S. Strano, Electronics and optoelectronics of two-dimensional transition metal dichalcogenides, Nat. Nanotechnol. **7**, 699 (2012).

[17] S. Manzeli, D. Ovchinnikov, D. Pasquier, O. V. Yazyev, and A. Kis, 2D transition metal dichalcogenides, Nat. Rev. Mater. **2**, 17033 (2017).

[18] W. Choi, N. Choudhary, G. H. Han, J. Park, D. Akinwande, and Y. H. Lee, Recent development of two-dimensional transition metal dichalcogenides and their applications, Mater. Today **20**, 116 (2017).

[19] G. H. Han, D. L. Duong, D. H. Keum, S. J. Yun, and Y. H. Lee, van der Waals metallic transition metal dichalcogenides, Chem. Rev. **118**, 6297 (2018).

[20] E. Marseglia, Transition metal dichalcogenides and their intercalates, Int. Rev. Phys. Chem. **3**, 177 (1983).

[21] J. A. Wilson, F. Di Salvo, and S. Mahajan, Charge-density waves and superlattices in the metallic layered transition metal dichalcogenides, Adv. Phys. **24**, 117 (1975).

[22] F. Soto, H. Berger, L. Cabo, C. Carballeira, J. Mosqueira, D. Pavuna, P. Toimil, and F. Vidal, Electric and magnetic characterization of $NbSe_2$ single crystals: Anisotropic superconducting fluctuations above T_c, Physica C **460–462**, 789 (2007).

[23] M. D. Johannes and I. I. Mazin, Fermi surface nesting and the origin of charge density waves in metals, Phys. Rev. B **77**, 165135 (2008).

[24] T. Yokoya, T. Kiss, A. Chainani, S. Shin, M. Nohara, and H. Takagi, Fermi surface sheet-dependent superconductivity in $2H$-$NbSe_2$, Science **294**, 2518 (2001).

[25] K. Rossnagel, O. Seifarth, L. Kipp, M. Skibowski, D. Voß, P. Krüger, A. Mazur, and J. Pollmann, Fermi surface of $2H$-$NbSe_2$ and its implications on the charge-density-wave mechanism, Phys. Rev. B **64**, 235119 (2001).

[26] S. V. Borisenko, A. A. Kordyuk, V. B. Zabolotnyy, D. S. Inosov, D. Evtushinsky, B. Büchner, A. N. Yaresko, A. Varykhalov, R. Follath, W. Eberhardt, *et al.*, Two energy gaps and fermi-surface "arcs" in $NbSe_2$, Phys. Rev. Lett. **102**, 166402 (2009).

[27] X. Xi, L. Zhao, Z. Wang, H. Berger, L. Forró, J. Shan, and K. F. Mak, Strongly enhanced charge-density-wave order in monolayer $NbSe_2$, Nat. Nanotechnol. **10**, 765 (2015).

[28] A. Wieteska, B. Foutty, Z. Guguchia, F. Flicker, B. Mazel, L. Fu, S. Jia, C. Marianetti, J. van Wezel, and A. Pasupathy, Uniaxial strain tuning of superconductivity in $2H$-$NbSe_2$, arXiv:1903.05253.

[29] F. O. von Rohr, J.-C. Orain, R. Khasanov, C. Witteveen, Z. Shermadini, A. Nikitin, J. Chang, A. R. Wieteska, A. N. Pasupathy, M. Z. Hasan, A. Amato, H. Luetkens, Y. J. Uemura, and Z. Guguchia, Unconventional scaling of the superfluid density with the critical temperature in transition metal dichalcogenides, Sci. Adv. **5**, eaav8465 (2019).

[30] Z. Guguchia, F. von Rohr, Z. Shermadini, A. T. Lee, S. Banerjee, A. Wieteska, C. Marianetti, B. Frandsen, H. Luetkens, Z. Gong, *et al.*, Signatures of the topological s^{+-} superconducting order parameter in the type-II Weyl semimetal T_d-$MoTe_2$, Nat. Commun. **8**, 1082 (2017).

[31] Y. Jung, Y. Zhou, and J. J. Cha, Intercalation in two-dimensional transition metal chalcogenides, Inorg. Chem. Front. **3**, 452 (2016).

[32] Z. Wang, R. Li, C. Su, and K. P. Loh, Intercalated phases of transition metal dichalcogenides, Smart. Mater. **1**, e1013 (2020).

[33] T. Moriya and T. Miyadai, Evidence for the helical spin structure due to antisymmetric exchange interaction in $Cr_{13}NbS_2$, Solid State Commun. **42**, 209 (1982).

[34] K. Suzuki, T. Kondo, T. Enoki, and S. Bandow, Conduction mechanism and two-dimensional magnetism in incommensurate layered compounds $(REs)_xMS_2$ (RE = rare earth metal, M = Ta, V), Synth. Met. **56**, 1741 (1993).

[35] Y. Kousaka, T. Ogura, J. Zhang, P. Miao, S. Lee, S. Torii, T. Kamiyama, J. Campo, K. Inoue, and J. Akimitsu, Long periodic helimagnetic ordering in CrM_3S_6 (M = Nb and Ta), J. Phys. Conf. Ser. **746**, 012061 (2016).

[36] A. Hall, D. Khalyavin, P. Manuel, D. Mayoh, F. Orlandi, O. Petrenko, M. R. Lees, and G. Balakrishnan, Magnetic structure investigation of the intercalated transition metal dichalcogenide $V_{1/3}NbS_2$, Phys. Rev. B **103**, 174431 (2021).

[37] C. Zhang, J. Zhang, C. Liu, S. Zhang, Y. Yuan, P. Li, Y. Wen, Z. Jiang, B. Zhou, Y. Lei, *et al.*, Chiral helimagnetism and one-dimensional magnetic solitons in a Cr-intercalated transition metal dichalcogenide, Adv. Mater. **33**, 2101131 (2021).

[38] T. Hicken, Z. Hawkhead, M. Wilson, B. Huddart, A. Hall, G. Balakrishnan, C. Wang, F. Pratt, S. Clark, and T. Lancaster, Energy-gap driven low-temperature magnetic and transport properties in $Cr_{1/3}MS_2$ (M = Nb, Ta), Phys. Rev. B **105**, L060407 (2022).

[39] L. S. Xie, S. Husremovic, O. Gonzalez, I. M. Craig, and D. K. Bediako, Structure and magnetism of iron- and chromium-intercalated niobium and tantalum disulfides, J. Am. Chem. Soc. **144**, 9525 (2022).

[40] F. Eder, C. Witteveen, E. Giannini, and F. O. von Rohr, Structural modulation and enhanced magnetic ordering in incommensurate $K_{1-x}CrSe_2$ crystals, J. Am. Chem. Soc. **147**, 4896 (2025).

[41] H. C. Mandujano, P. Y. Zavalij, A. Manjón-Sanz, H. Cao, and E. E. Rodriguez, Coexistence of commensurate and incommensurate antiferromagnetic ground states in Co_xNbSe_2 single crystal, Phys. Rev. Mater. **9**, 014403 (2025).

[42] A. Amato, H. Luetkens, K. Sedlak, A. Stoykov, R. Scheuermann, M. Elender, A. Raselli, and D. Graf, The new versatile general purpose surface-muon instrument (GPS) based on silicon photomultipliers for μSR measurements on a continuous-wave beam, Rev. Sci. Instrum. **88**, 093301 (2017).

[43] R. Kubo and T. Toyabe, Magnetic resonance and relaxation, in *Proceedings of the 14th Colloque Ampère*, edited by R. Blinc (North-Holland, Amsterdam, 1967).

[44] A. Yaouanc and P. D. De Reotier, *Muon Spin Rotation, Relaxation, and Resonance: Applications to Condensed Matter* (Oxford University Press, Oxford, 2011), Vol. 147.

[45] S. J. Blundell, R. de Renzi, T. Lancaster, and F. L. Pratt, *Muon Spectroscopy: An Introduction* (Oxford University Press, New York, 2022).

[46] S. Blundell and T. Lancaster, DFT + μ: Density functional theory for muon site determination, Appl. Phys. Rev. **10**, 021316 (2023).

[47] B. Huddart, A. Hernández-Melián, T. Hicken, M. Gomilšek, Z. Hawkhead, S. Clark, F. Pratt, and T. Lancaster, MuFinder: A program to determine and analyse muon stopping sites, Comput. Phys. Commun. **280**, 108488 (2022).

[48] Z. Hawkhead, T. Hicken, N. Bentley, B. Huddart, S. Clark, and T. Lancaster, Band-filling-controlled magnetism from transition metal intercalation in $N_{1/3}NbS_2$ revealed with first-principles calculations, Phys. Rev. Mater. **7**, 114002 (2023).

[49] A. Suter and B. Wojek, Musrfit: A free platform-independent framework for μSR data analysis, Phys. Procedia **30**, 69 (2012).

[50] S. J. Clark, M. D. Segall, C. J. Pickard, P. J. Hasnip, M. I. Probert, K. Refson, and M. C. Payne, First principles methods using CASTEP, Z. Kristallogr. Cryst. Mater. **220**, 567 (2005).

[51] J. P. Perdew, A. Ruzsinszky, G. I. Csonka, O. A. Vydrov, G. E. Scuseria, L. A. Constantin, X. Zhou, and K. Burke, Restoring the density-gradient expansion for exchange in solids and surfaces, Phys. Rev. Lett. **100**, 136406 (2008).

[52] H. J. Monkhorst and J. D. Pack, Special points for Brillouin-zone integrations, Phys. Rev. B **13**, 5188 (1976).

[53] P. Bonfà, I. J. Onuorah, and R. De Renzi, Introduction and a quick look at MUESR, the magnetic structure and mUon

embedding site refinement suite, JPS Conf. Proc. **21**, 011052 (2018).

[54] A. Amato and E. Morenzoni, *Introduction to Muon Spin Spectroscopy: Applications to Solid State and Material Sciences* (Springer, Cham, Switzerland, 2024).

[55] K. J. Franke, B. M. Huddart, T. J. Hicken, F. Xiao, S. J. Blundell, F. L. Pratt, M. Crisanti, J. A. Barker, S. J. Clark, A. Štefančič, *et al.*, Magnetic phases of skyrmion-hosting $GaV_4S_{8-y}Se_y$ (y = 0, 2, 4, 8) probed with muon spectroscopy, Phys. Rev. B **98**, 054428 (2018).

[56] G. Luke, J. Brewer, S. Kreitzman, D. Noakes, M. Celio, R. Kadono, and E. Ansaldo, Muon diffusion and spin dynamics in copper, Phys. Rev. B **43**, 3284 (1991).